pp 702–719.
doi:10.1017/aer.2020.120

Influence of distorted inflows on the performance of a contra-rotating fan

M.P. Manas and A.M. Pradeep
manump9@gmail.com
Department of Aerospace Engineering
Indian Institute of Technology Bombay
Mumbai
India

ABSTRACT

A contra-rotating fan offers several aerodynamic advantages that make it a potential candidate for future aircraft engine configurations. Stall in a contra-rotating axial fan is interesting since instabilities could arise from either or both of the rotors. In this experimental study, a contra-rotating axial fan is analysed under clean or distorted inflow conditions to understand its performance and stall inception characteristics. The steady and unsteady measurements identified the relative contribution of each rotor towards the performance of the stage. The tip of rotor-1 is identified to be the most critical region of the contra-rotating fan. The contribution of rotor-2 to the overall loading of the stage is observed to be relatively less than rotor-1. The penalty due to distortion in the stage pressure rise is mostly felt by rotor-1, while rotor-2 also shows a reduction in performance for distorted inflows. Rotor-2 stalls at a high flow coefficient marking the initiation of partial stall of the stage, and the stall of the whole stage occurs once rotor-1 stalls. A fluid phenomenon that is attached to the blade surface marks the stall of rotor-1, and this fluid phenomenon initially rotates at a speed close to the speed of rotation of the blade. As the stage moves towards the fully developed stall, this fluid phenomenon sheds from the blade surface. The fluid phenomenon thus propagates at a speed much lower than the rotational speed of the blade during fully developed stall.

Keywords: Contra-rotating fan; axial compressor; Stall and surge; Unsteady flows

NOMENCLATURE

C_a	axial velocity, m/s
f	frequency, Hz
M	Mach number
$\dot{m}$	mass flow rate, kg/s
N_d	design rotational speed, RPM

Received 20 April 2020; revised 23 September 2020; accepted 6 October 2020.

P	static pressure, Pa
P_0	total pressure, Pa
U_{mid}	rotational speed of blade at mid-span, m/s
Z	number of samples

Greek symbols

β	flow angle, degrees
γ	stagger, degrees
ϕ	flow coefficient $= \frac{C_a}{U_{mid}}$
ψ	loading coefficient $= \frac{P_{0,station} - P_{0,11}}{\rho U_{mid}^2}$
ρ	density, kg/m^3
σ	solidity

Abbreviations

BPF	blade passing frequency
CRAF	contra-rotating axial fan
DF	diffusion factor
FFT	fast Fourier transform
LLSD	long-length-scale disturbance
SLSD	short-length-scale disturbance

Subscript

station	any axial position
mid	mid-span
R1	rotor-1
R2	rotor-2

1.0 INTRODUCTION

A Contra-Rotating Axial Fan (CRAF) offers potential aerodynamic advantages when substituting the conventional fan of an aircraft engine. In this study, a CRAF with a low hub–tip ratio and low aspect ratio was investigated. Recently, designers have considered the possibility of implemeting such fans with low hub–tip ratio for turbofan engines[1]. A configuration with a low hub–tip ratio will lead to a reduction in the maximum diameter of the fan and thus reduce the weight while increasing the fan efficiency. Low-aspect-ratio fans have been the choice of designers over the past few decades owing to their various aerodynamic and structural advantages[2]. In a contra-rotating configuration, the two rotors rotate in opposite directions and the stage develops a larger pressure rise compared with a traditional fan. Moreover, a CRAF can provide a swirl-free discharge, and the rotors can be designed to operate at different speed combinations to achieve optimum performance. CRAFs have not yet been successfully implemented in commercial aircraft engines due to mechanical limitations, but they represent potential candidates for use in future aircraft engines that demand high stage pressure rises. A high stage pressure rise leads to improved specific fuel consumption (SFC) and thus increases the overall efficiency of the engine. Moreover, if the stage pressure ratio is higher,

https://doi.org/10.1017/aer.2020.120 Published online by Cambridge University Press

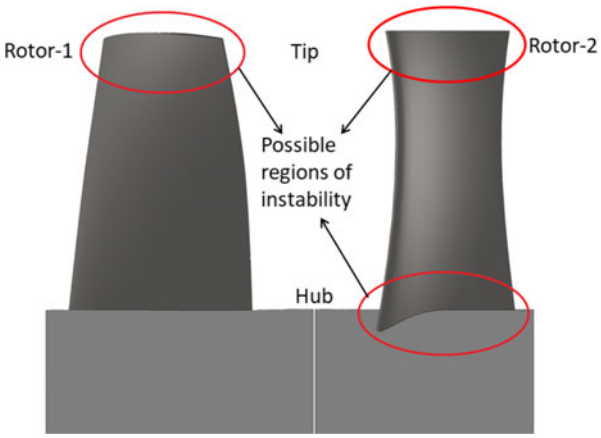

Figure 1. Illustration of the regions of instability in a CRAF.

the overall size of the engine can be reduced. Several recent studies have aimed to develop and understand distortion-tolerant fans for future aircraft engine configurations[3-7]. For such configurations, it is important to understand the regions of the fan that are intolerant to inflow distortions. Distortion can occur due to several adverse effects at take-off, climb, cruise or landing; For example, the engine may receive distorted inflows if the flight undergoes a high angle-of-attack manoeuvre at take-off, or due to air turbulence during cruise. In a CRAF, the two rotors constitute one stage and instabilities leading to stall could arise from either or both of the rotors. The typical regions of instability in a CRAF are illustrated in Fig. 1. The effects of inflow distortion, stall inception and the design and performance of CRAF must be understood to improve an existing CRAF design. Stall is an instability which results in flow breakdown, originally developing due to the adverse pressure gradient in compressors and fans. In situations where the operating mass flow rate of a fan is low, the fan back pressure increases, as does the angle of incidence to the blade. This can lead to large separations on the blade surface and ultimately to flow reversal. During actual flight, such situations can occur due to air turbulence, high angle-of-attack manoeuvres, bird hits, wind gusts, etc., which distort the inflow to the fan. Thus, one of the common causes for the occurrence of stall in a compressor or fan is when the incidence of the flow on the blade exceeds the critical incidence, leading to flow separation. Stall also occurs due to local instabilities and can disrupt the flow locally. Stall results in a significant reduction in the pressure ratio and efficiency of the compression system. If not mitigated, stall can lead to severe vibratory stresses on the blade, resulting in critical damage to the engine. A brief review of previous studies on the stall phenomenon in compressors and fans, the effect of non-uniform inflows and the general performance of CRAFs is summarised below.

The pioneering explanation for stall initiation in an axial compressor was given by Emmons et al.[8]. The conceptual model identified that stall basically develops due to large positive incidences on the blade at low mass flow rates. In later studies, stall was explained based on theoretical models, which predict the basic evolution of rotating stall[9]. Thereafter, most works started to focus on rigorous experimentation based on advances in measurement and post-processing techniques. McDougall et al.[10] identified Short-Length-Scale Disturbances (SLSD) or spikes and Long-Length-Scale disturbances (LLSD) or modal waves prior to the development of fully developed stall, and Garnier et al.[11] verified the presence of pre-stall

https://doi.org/10.1017/aer.2020.120 Published online by Cambridge University Press

waves in compressors and their ability to act as stall precursors. The pre-stall waves precede stall cell formation and were found to have a connection with the fully developed stall cells. Further studies confirmed the existence of SLSD and LLSD[12,13]. Work on stall inception continues to rely on experimentation, although recently further insight into the interior flow field has been obtained using numerical simulations.

Over the past few decades, several works have focused on understanding the performance characteristics of CRAF. One of the early works, an experimental study on a low-speed CRAF, identified that stall on rotor-1 can be suppressed if rotor-2 is operated at a comparatively higher speed than rotor-1[14]. This phenomenon was observed in several subsequent studies as well. Roy et al.[15] reported that, at flow coefficients close to stall, large incidences on rotor-2 at low mass flow rates lead to separation on the blade surface. One later study concluded that, at lower rotational speeds of rotor-1, rotor-2 suffers separation on the pressure surface due to high negative incidence angles[16]. Thus, operating rotor-2 at speeds higher than rotor-1 and the design speed extends the stall margin of the stage. Moreover, the performance of each rotor revealed that rotor-2 has a lower stall margin compared with rotor-1. A lnumerical and experimental study[17] concluded that instabilities leading to stall arise primarily on rotor-1. A study on the performance characteristics of a CRAF was later carried and concluded that a CRAF has two stall zones, namely partial stall, which corresponds to the stall of rotor-2, and full stall, which corresponds to the stall of the stage[18]. Unsteady experimental studies[19,20] carried out on a CRAF revealed that fully developed stall is preceded mostly by LLSD. However, intermittent SLSD appeared along with the LLSD. Numerical simulations and unsteady experiments on a low-aspect-ratio CRAF concluded that the strong suction of rotor-2 drags the tip-leakage vortex (TLV) of rotor-1 to the axial direction and thereby suppresses the rotating stall[21].

During the initial phases of engine development, studies on the effect of non-uniform inflows focus on understanding the attenuation of distortion across the stage[22]. Later, studies on the radial, circumferential and complex distortion patterns are carried out. One of the studies on radial distortions[23] revealed that certain hub-radial distortion conditions show a wider stable operating margin than other inflow conditions. However, this trend is not general, since another study observed that hub-radial and tip-radial distortion patterns show inferior performance in terms of the pressure rise capability and stability margin characteristics[24]. A later study reported the flow features under inflow distortions[25], while another study modelled the inflow distortions using parallel compressor theory[26,27]. Gunn et al.[28] investigated the effect of circumferential distortion on a fan stage operating at low speeds, reporting significant efficiency losses as a result of the large incidences on the blades along the entire annulus. A study on an axial fan with radial distortion blades identified that the modal waves leading to stall had a significant effect due to the flow near the hub region[29]. A few recent works have analyzed the characteristics of a high-aspect-ratio CRAF under radial and circumferential distortions[30,31]. Generally, radial and circumferential distortions reduce the loading and the stability margin of the stage. However, tip-radial distortion resulted in a small improvement in loading at certain flow coefficients[30]. Under circumferential distortion, the distorted region of the flow initially propagates in the direction of rotation of rotor-1 as the flow crosses rotor-1, and later in the direction of rotation of rotor-2 as the flow crosses rotor-2. During stall inception, SLSD were observed within LLSD, and strong casing pressure fluctuations and the stall cell frequency amplitude were observed[20]. A study on the unsteady behaviour of a CRAF under radially distorted inflow conditions was carried out by Manas and Pradeep[32], who identified both LLSD and SLSD during stall inception. The tip-distorted flow condition mostly showed SLSD, and the study could not identify any significant disturbance on rotor-2.

https://doi.org/10.1017/aer.2020.120 Published online by Cambridge University Press

Table 1
Specifications of rotor-1

Parameter	Hub	Mid	Tip
ψ_{R1}	0.19	0.55	0.69
θ_{R1}	30.60°	33.49°	17.76°
γ_{R1}	11.88°	31.79°	49.21°
DF_{R1}	0.27	0.58	0.51

Table 2
Specifications of rotor-2

Parameter	Hub	Mid	Tip
ψ_{R1FB}	0.15	0.50	0.60
θ_{R2}	39.40°	38.26°	37.52°
γ_{R2}	44.69°	56.45°	49.50°
DF_{R2}	0.30	0.49	0.41

Based on previous work carried out on CRAFs, it can be concluded that the flow dynamics associated with stall for CRAFs is not thoroughly understood. This paper, hence, tries to analyze the critical regions in a low-speed CRAF subject to various inflow conditions, such as clean flow, hub-radial distortion, tip-radial distortion and simple circumferential distortion. The CRAF has a low hub–tip ratio and low aspect ratio. A low hub–tip ratio can lead to a reduction in the overall size of the fan. Thus, the weight of the engine can be reduced and the efficiency of the fan improved[1]. Similarly, the use of a blade with an aspect ratio between 1 and 1.5 has been found to result in higher efficiency than high-aspect-ratio blades[33]. Since the CRAF operates at low speeds, the Reynolds number is considerably to be lower than that observed in typical gas turbines, and the Mach number associated with the flow is in the low subsonic regime. Nevertheless, the fundamental flow features identified in this study provide a preliminary understanding of the behaviour of the two rotors and the stall inception phenomenon in CRAFs. Moreover, this study also identifies the relative contribution of each rotor to stall. Identifying the critical regions and the individual performance of the two rotors may help when choosing better design strategies to develop distortion-tolerant CRAFs for use in future gas turbine engines.

2.0 METHODOLOGY

Experiments were carried out at a CRAF facility designed to deliver a loading coefficient of 1.05 at the mid-span at a flow coefficient of 0.79. A schematic and photograph of the test facility are shown in Fig. 2. The Reynolds number calculated from the reference chord length and reference axial velocity is approximately 2×10^5. The rotors are operated under the design speed combination $N_d - N_d$. The major design specifications of the rotors are presented in Tables 1 and 2, and the parameters of the test rig are given in Table 3.

Inflow distortions were realised using wired mesh screens. The presence of a screen delivers flow with a low total pressure to the fan. The screens are placed at the inlet of the stage, at

https://doi.org/10.1017/aer.2020.120 Published online by Cambridge University Press

Table 3
Parameters of the test rig

Parameter	Rotor-1	Rotor-2
Number of blades	9	7
Hub–tip ratio	0.33	0.33
Aspect ratio	1.5	1.5

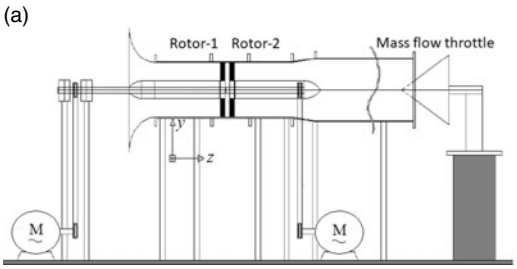

Schematic of the test facility

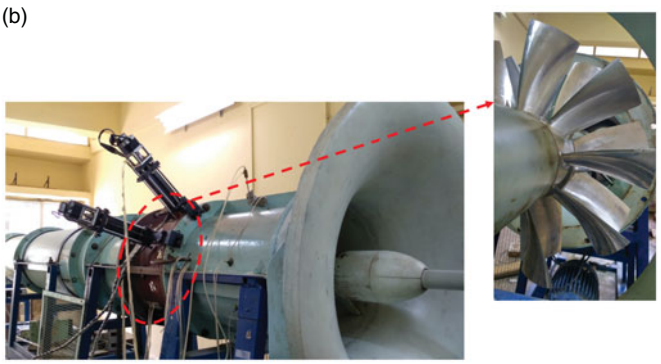

Photograph of the test facility

Figure 2. Schematic and photograph of the test rig.

a distance of 2.84 times the casing radius from rotor-1. The wired mesh screens for the hub-radial distortion and the tip-radial distortion conditions extend up to 0.33% of the span from the hub and 0.2% of the span from the tip, respectively[30]. The wired mesh screen for the simple circumferential distortion condition extends to 90°. The meshes used for the radial and the circumferential distortion conditions have a porosity of 0.69.

Total pressure measurements were carried out with the help of Pitot rakes, Kiel probe rakes and seven-hole probes. The probes were positioned 90° apart on the annulus. The measurements were recorded at the stage inlet, in between the two rotors, and at the stage exit. To determine the radial and circumferential distributions of the total pressure, the seven-hole probe was traversed radially from the tip to the hub at four circumferential locations 90° apart. The annular loading distribution for the circumferential distortion was obtained by interpolating the recorded data. The stall inception phenomenon was captured from the pressure measurements recorded at the casing using Kulite ET-3DC-312 (M) series high-response

https://doi.org/10.1017/aer.2020.120 Published online by Cambridge University Press

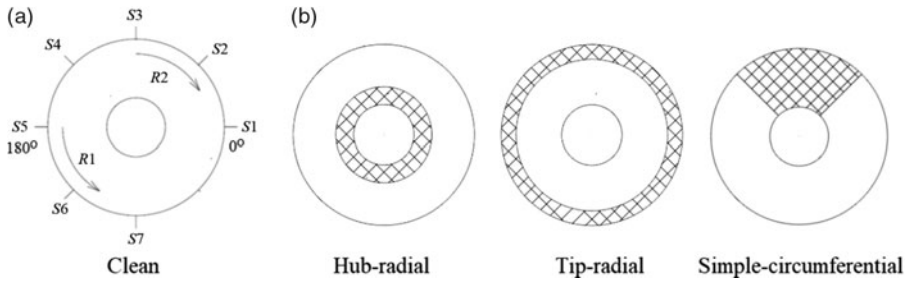

Figure 3. Schematic of the (a) sensor positions and (b) distortion configurations.

sensors arranged circumferentially close to the leading edge of the rotors and sampled at a frequency of 10kHz. The uncertainty in the pressure measurements obtained for the steady measurements using the pressure scanners is ± 0.05% of full scale, and for the unsteady measurements using the pressure sensors is ±0.5%. Schematics of the distortion screens and the sensor positions are illustrated in Fig. 3.

A standard fifth-order Butterworth filter was applied to the pressure data to capture the most significant frequencies associated with the recorded data. The stall inception phenomenon was analysed based on the raw pressure traces, wavelet analysis and Fourier analysis techniques. Here, 'Time (rotor revs.) = 0' represents the initiation of fully developed stall, and the stall inception phenomenon is analysed from 'Time (rotor revs.) = −300' to 'Time (rotor revs.) = 30'. At certain instances, the larger time windows are broken down into smaller windows to provide further insight into the pre-stall phenomenon.

The Morlet wavelet transform was further applied to help identify the phenomenon occurring during the stall inception process. As the raw data, which are a function of time, are converted into time–frequency space, both the dominant modes and their variation in time can be identified. Wavelet analysis thus provides meaningful information on the pre-stall phenomenon and associated frequency bands. In this paper, wavelet analysis was carried out on the raw, unfiltered data, thereby capturing all significant frequencies present in the flow. The expression for the Morlet mother wavelet consists of a normal wave transformed by a Gaussian.

$$\chi_0(\eta) = \pi^{-\frac{1}{4}} e^{i\omega_0\eta} e^{\frac{-\eta^2}{2}} \quad \ldots(1)$$

Here, the wavelet function $\chi_0(\eta)$ depends on η, a non-dimensional parameter of time. x_n and ω_0 denote the time series and the non-dimensional frequency, respectively. The expression for the continuous wavelet transform of the time series x_n is:

$$W_n(s) = \sum_{n=0}^{N-1} x_{n'} \chi^* \left[\frac{(n'-n)\delta t}{s} \right] \quad \ldots(2)$$

The above equation expresses the convolution of the time series x_n with a form of the wavelet function which is scaled and translated. By choosing a suitable scale and translation length, the variation of the amplitude with time can be identified. All N convolutions can be

https://doi.org/10.1017/aer.2020.120 Published online by Cambridge University Press

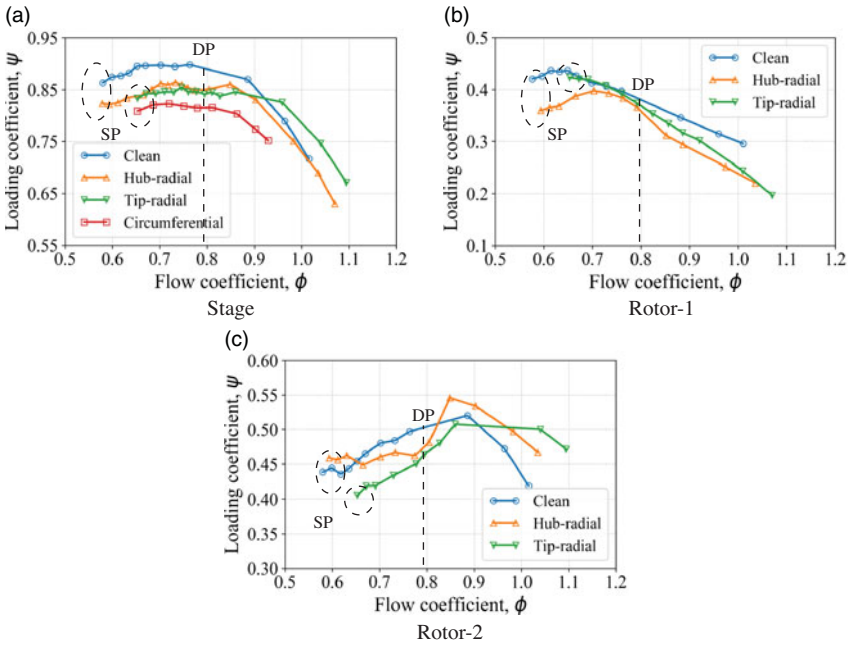

Figure 4. Performance for various inflow conditions. The dashed line marks the design point (DP), while the dashed circles show the stall points (SP).

carried out at the same time using the discrete Fourier transform (DFT). The DFT of the time series x_n is expressed as

$$\hat{x_k} = \frac{1}{N}\sum_{n=0}^{N-1} x_n e^{\frac{-2\pi ikn}{N}} \quad \ldots (3)$$

The following equation can be used to obtain the wavelet coefficients:

$$W_n(s) = \sum_{k=0}^{N-1} \hat{x}_k \hat{\chi} * (s\omega_k) e^{i\omega_k n\delta t} \quad \ldots (4)$$

Here, χ is a function of the mother wavelet, W is the wavelet coefficient, s is the scale, N is the total number of samples, k is the frequency index, η is non-dimensional time and the overhat symbol indicates the fast Fourier transform of the respective parameter. The wavelet coefficients are determined for the unfiltered data, hence the analysis identifies phenomena occurring in all frequency bands. This method is explained in detail in Ref. [34].

3.0 RESULTS AND DISCUSSION

A comparison of the loading characteristics of the stage for various inflow conditions is shown in Fig. 4. The highest loading at the design point and a considerable stall margin are observed for the clean inflow condition. It is observed that the inflow distortions have a significant

https://doi.org/10.1017/aer.2020.120 Published online by Cambridge University Press

effect on the stage loading and stall margin. Although the hub–radial distortion has a lower loading compared with the clean inflow condition, the stall mass flow rate is nearly the same in both cases. Among the radial distortions, the tip-radial distortion appears to affect the stage performance more severely. The loading coefficient and stall flow coefficient for the case of tip-radial distortion are much lower compared with the clean inflow condition. Compared with the radial distortions, the simple circumferential distortion affects the performance of the stage more drastically. The loading coefficient of the simple circumferential distortion is the lowest among all the inflow conditions. For the simple circumferential non-uniformities, one or more inter-blade channels are completely distorted, whereas for the radial non-uniformities, only a part of the span of every blade is distorted while the other parts of the span continue to add work to the flow. Thus, in general, the clean inflow delivers the largest stage loading, followed by the radial distortions and finally the simple circumferential distortion.

The loading coefficients of rotor-1 and rotor-2 are shown in Fig. 4. For rotor-1, the clean inflow condition delivers the highest loading while the hub-radial distortion delivers the lowest. With a reduction in the flow coefficient, the loading coefficient increases up to a flow coefficient of 0.65 for the clean inflow, 0.7 for the hub-radial distortion and 0.65 for the tip-radial distortion condition. From these peak pressure points of rotor-1, the loading coefficients drop towards lower flow coefficients until the stage stalls, except under the tip-radial distortion condition, which stalls at the peak pressure point of rotor-1. A comparison of the performance of rotor-1 with that of the stage shows that the peak pressure points of rotor-1 and the stage are different for the different inflow conditions. For instance, the peak pressure point of the clean inflow condition of rotor-1 is 0.65 while that of the stage is 0.75. Thus, rotor-1 tries to increase the pressure rise, but this is not reflected in the overall loading of the stage. This means that the pressure rise developed by rotor-1 is negated by the pressure rise developed by rotor-2. The loading coefficient of rotor-2 for all the inflow conditions starts to decrease starting at a flow coefficient lower than the design flow coefficient. The peak pressure point in the case of rotor-2 is thus observed at flow coefficients higher than the design flow coefficient. The clean, hub-radial and tip-radial inflow conditions show a significant reduction in loading from the peak pressure point towards the stall point. The hub-radial distortion delivers a slightly higher pressure rise in comparison with the clean inflow condition at higher flow coefficients. However, starting from a flow coefficient close to the design flow coefficient towards low flow coefficients, the clean inflow condition shows a higher pressure rise than the hub-radial distortion condition. Thus, it can be inferred that rotor-2 cannot deliver a high pressure rise at low flow coefficients while rotor-1 provides a larger contribution to the overall stage loading. Comparing the performance of the stage and the individual rotors, it is thus confirmed that rotor-1 performs relatively better than rotor-2 and that the performance of the individual rotors is reflected in the performance of the stage. As the loading coefficient of rotor-2 for all the inflow distortions starts to drop before the design point, rotor-2 will probably stall earlier, resulting in partial stall of the stage. However, the stage continues to show an increase in the loading coefficient up to a mass flow rate close to the stall mass flow rate. This is because rotor-1 continues to increase the loading coefficient until reaching a flow coefficient close to stall. Here, the ability of rotor-1 to increase the loading up to low flow coefficients is also due to the effect of the suction by rotor-2, which helps the flow to remain attached on rotor-1. Complete stall of the stage occurs when rotor-1 stalls due to instabilities occurring near the tip region of rotor-1.

Figure 5 shows the inlet total pressure profiles expressed in terms of the loading coefficient, for the clean and radial distortion inflow conditions. The clean inflow condition has a nearly uniform loading distribution at the stage inlet. The hub-radial and tip-radial distortion inflow conditions have low total pressure values near the hub and tip regions, respectively. The effect

https://doi.org/10.1017/aer.2020.120 Published online by Cambridge University Press

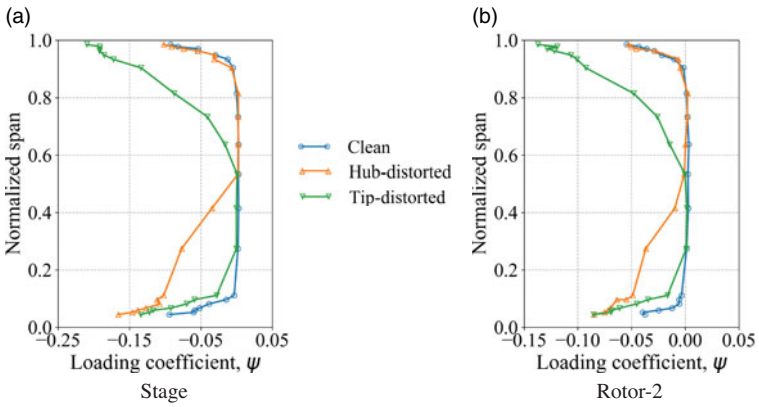

Figure 5. Spanwise loading coefficient at the stage inlet under clean and radial distorted inflow conditions.

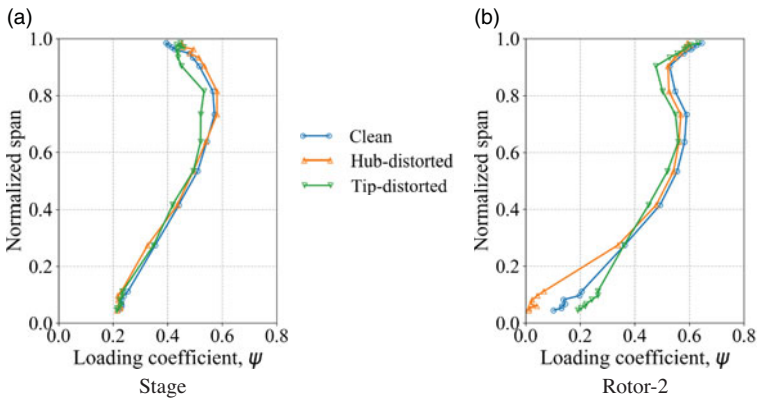

Figure 6. Spanwise loading coefficient at rotor-1 exit under clean and distorted inflow conditions.

of distortion is directly felt up to the mid-span for both the hub-radial and tip-radial distortion conditions. Therefore, the bottom regions of the span of rotor-1 receive a low-total-pressure inflow for the hub-radial distortion condition, while the top regions of the span of rotor-1 receive a low-total-pressure inflow for the tip-radial distortion inflow condition. The effect of the distortion is larger at the design point than at the stall point.

The distributions of the loading coefficient at the rotor-1 exit for the clean, hub-radial and tip-radial distortion inflow conditions appear to be very similar, as shown in Fig. 6. The tip-radial distortion condition delivers a slightly lower loading coefficient close to the tip region compared swith the other inflow conditions. Similarly, the hub-radial distortion condition shows a lower loading coefficient near the hub region compared with the other inflow conditions.

Furthermore, all the inflow conditions deliver very similar profiles as the flow develops across rotor-2. However, although it appears that the loading coefficient profiles at the exit of rotor-1 are identical under all the inflow conditions, the flow non-uniformities at the inlet do affect the performance of rotor-2 also (Fig. 4). Note that the radial distortion conditions have a significant impact on the stage performance, as seen in Fig. 4. Figure 7 depicts the spanwise loading distribution at the stage exit. The loading distribution appears to be nearly

https://doi.org/10.1017/aer.2020.120 Published online by Cambridge University Press

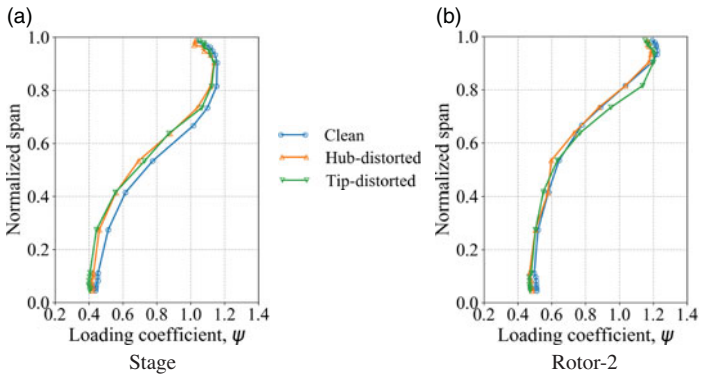

Figure 7. Spanwise loading coefficient at the stage exit under clean and distorted inflow conditions.

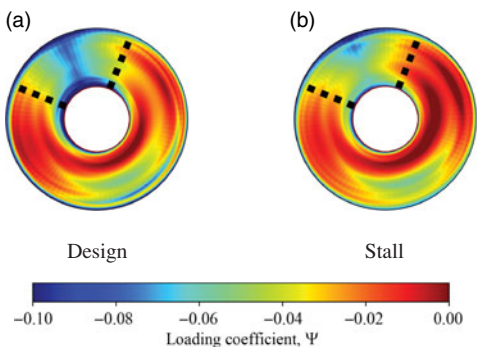

Figure 8. Loading coefficient at the inlet of stage under simple circumferential distortion. The 90° distortion screen spans between the dashed lines.

identical for all the inflow conditions. However, a slight reduction in the distribution of the loading along the span is observed for the distorted inflow conditions throughout the span. Therefore, the radial distortions do not significantly alter the loading distribution at the stage exit, although there is an overall reduction in the loading coefficient.

The flow development across the stage inferred from the spanwise loading distributions confirms that the loading distributions are nearly identical at the exit of the rotors. This confirms that a severe penalty due to distortion affects the performance of rotor-1. However, as seen in Fig. 4, radial distortions affect the performance of rotor-2 as well. Therefore, the hub-radial and tip-radial distortion conditions affect the performance of both rotors, which is reflected in the performance of the stage.

The radial distribution of the loading across the rotors of the CRAF is such that the hub is loaded less and the tip is loaded more. Therefore, the tip-radial distortion inflow condition will affect the performance to a much greater extent than the hub-radial distortion inflow condition. From the inlet profiles of the radial distortions, it can be expected that the tip-radial distortion inflow condition will stall earlier than the hub-radial distortion inflow condition. However, the loading at the design point is slightly higher for tip-radial distortion compared with hub-radial distortion (Fig. 4).

https://doi.org/10.1017/aer.2020.120 Published online by Cambridge University Press

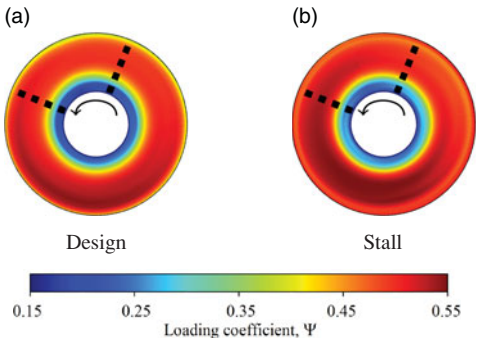

Figure 9. Loading coefficient at rotor-1 exit under simple circumferential distortion. The curved arrow shows the direction of rotation of rotor-1. The 90° distortion screen spans between the dashed lines.

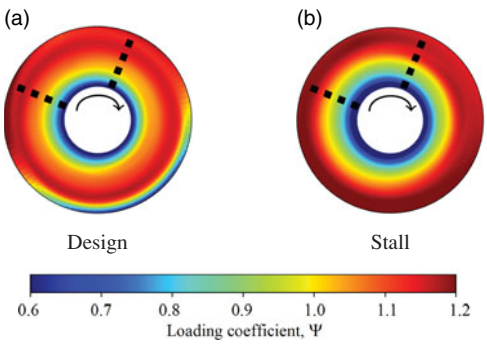

Figure 10. Loading coefficient at the stage exit under simple circumferential distortion. The 90° distortion screen spans between the dashed lines. The curved arrow shows the direction of rotation of rotor-2.

The loading coefficients at the stage inlet, rotor-1 exit and stage exit for the simple circumferential distortion condition are shown in Figs. 8, 9 and 10, respectively. The distortion screen spans between 67.5 and 157.5, thus the effect of the distortion at the inlet is immediately felt between 67.5 and 157.5, as illustrated in Fig. 8, with a gradual reduction in the effect of the distortion being observed towards other annular regions. The circumferential extent of the distortion is greater close to the hub region. The extent of the circumferential distortion propagates in the direction of rotation of rotor-1, and the loading coefficient distribution appears to be nearly equally spread across the complete annulus (Fig. 9). Thus, the simple circumferential distortion inflow condition will affect the performance of rotor-2. As the flow develops across rotor-2, the distortion propagates in the direction of rotation of rotor-2, and finally at the stage, the circumferential distributions of the loading coefficient appear to be nearly equal. Therefore, the simple circumferential distortion inflow condition also shows a nearly uniform annular distribution of the loading coefficient at the stage exit.

Figure 11 shows the pressure traces recorded at the casing during stall inception under the clean inflow condition. The unsteady pressure data recorded at the casing give an idea of the instabilities that occur as the stage moves to fully developed stall. The initial set of pre-stall disturbances is visible at around −200 rotor revolutions. The frequency of appearance and the strength of these waves increase towards fully developed stall. As the stage approaches stall, these waves appear more frequently and their strength increases. A set of pre-stall waves is

https://doi.org/10.1017/aer.2020.120 Published online by Cambridge University Press

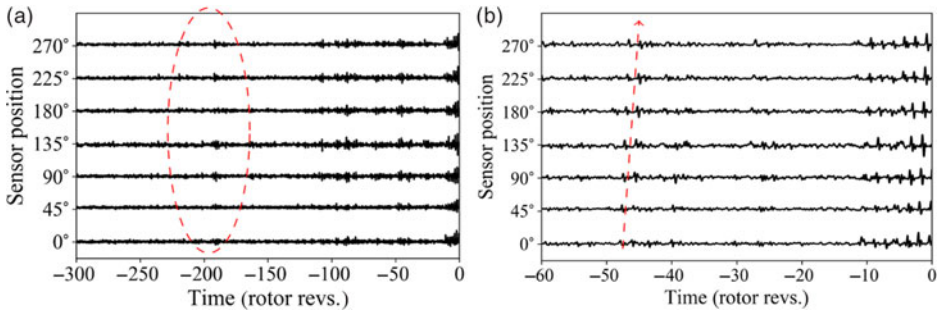

Figure 11. Pressure traces recorded at the casing under the clean inflow condition: (a) prior to stall and (b) immediately prior to stall. The data were recorded close to the leading edge of rotor-1 and were low-pass filtered at 0.33BPF. The migration of pre-stall waves along the annulus is indicated by the red dashed arrow.

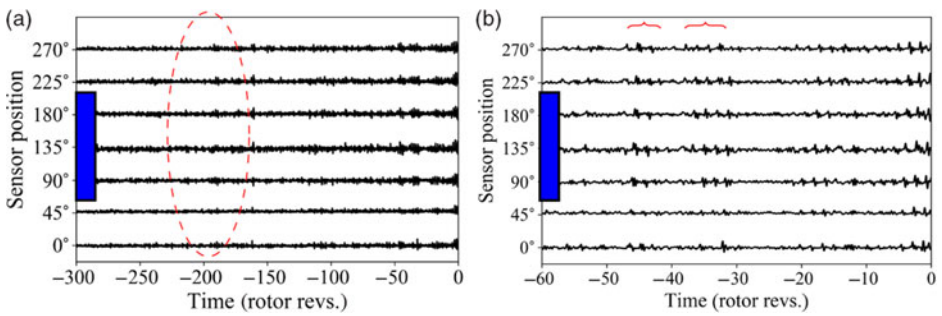

Figure 12. Pressure traces recorded at the casing during stall inception under simple circumferential inflow condition: (a) prior to stall, (b) immediately prior to stall. The data were recorded close to rotor-1 leading edge and were low-pass filtered at 0.33BPF. The rectangular box close to the abscissa shows the position of the distortion screen. The curly braces indicate the temporal extent of a set of pre-stall waves.

seen at approximately -100 rotor revolutions, and another set of waves is seen at approximately -50 rotor revolutions. Since the sensors are located on the casing close to the rotor-1 leading edge, it can be confirmed that these waves originate from the tip region of rotor-1. The pre-stall waves clearly appear to increase as the stage nears the fully developed stall regime.

Figure 12 shows the pressure data recorded close to the leading edge of rotor-1 under the simple circumferential distortion inflow condition. Compared with the clean inflow condition, the pre-stall waves under the simple circumferential distortion condition are stronger. The position of the distortion screen (shown by a blue rectangle close to the abcissa) affects the appearance of the pre-stall waves. However, the prestall waves appear to originate in the distorted sectors and grow in the direction of rotation of rotor-1. Closer inspection of these disturbances confirms that they are not sustained for too long and damp out within five rotor revolutions.

Figures 13 and 14 show the pressure data recorded close to the rotor-2 leading edge under the clean and simple circumferential distortion inflow conditions. The rotor-1 exit shows severe flow unsteadiness, which makes it difficult to predict the pre-stall behaviour of rotor-2. However, the rotor-2 tip region is less sensitive compared with the tip region of rotor-1, because the unsteady pressure data do not reveal any additional phenomena other than those occurring on rotor-1. Also, the simple circumferential distortion shows a higher frequency of

https://doi.org/10.1017/aer.2020.120 Published online by Cambridge University Press

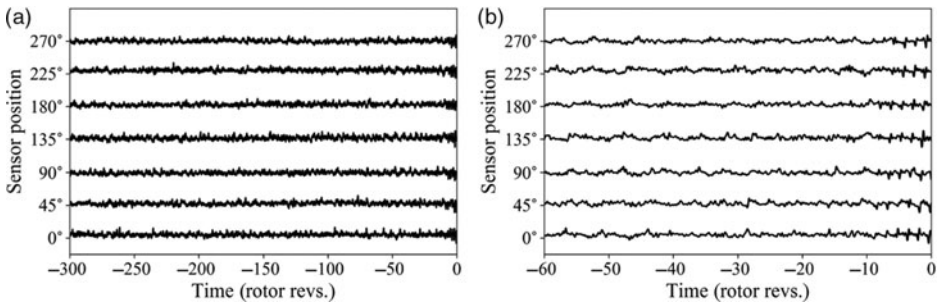

Figure 13. Pressure traces recorded at the casing during stall inception udner clean inflow condition: (a) prior to stall, (b) immediately prior to stall. The data were recorded close to the leading edge of rotor-2 and were low-pass filtered at 0.33BPF. The rectangular box close to the abscissa shows the position of the distortion screen.

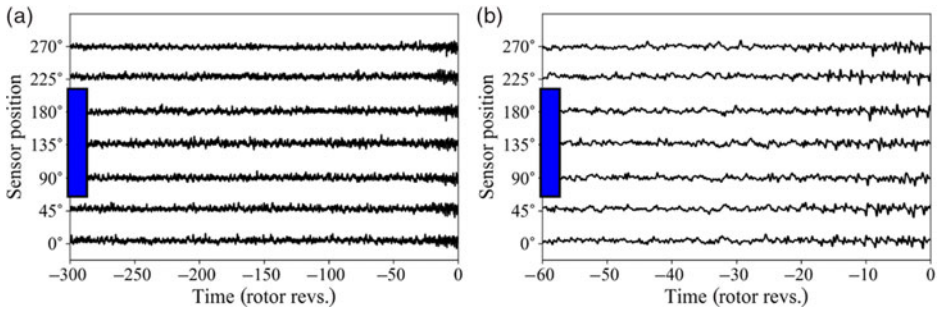

Figure 14. Pressure traces recorded at the casing during stall inception under the simple circumferential inflow condition: (a) prior to stall, (b) immediately prior to stall. The data were recorded close to the rotor-2 leading edge and were lowpass filtered at 0.33BPF. The rectangular box close to the abscissa shows the location of the distorted sector.

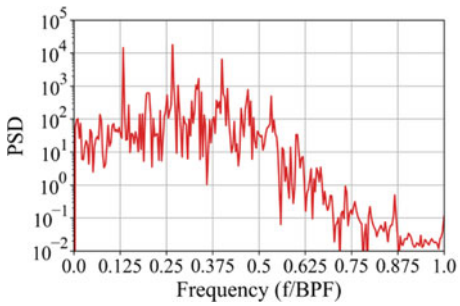

Figure 15. Power spectral density under simple circumferential distortion condition during fully developed stall.

disturbances on rotor-2 during the fully developed stall, which is identical to that observed on rotor-1. Therefore, the casing static pressure traces identified on rotor-2 are affected by the phenomenon occurring on rotor-1.

Figure 15 shows the power spectral density (PSD) under the simple circumferential distortion condition during fully developed stall. The fundamental frequency of the stall cells

https://doi.org/10.1017/aer.2020.120 Published online by Cambridge University Press

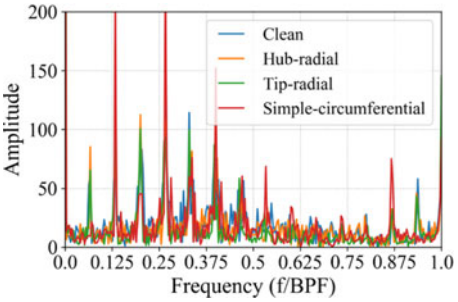

Figure 16. FFT during fully developed stall.

is 0.125BPF. Much of the higher-amplitude stall inception phenomenon is associated with low frequencies. These frequencies, therefore, correspond to the stall cell frequency, and the energy associated with the fluid is lost wehn these disturbances are generated.

The stall cell frequency for all the inflow conditions is shown in Fig. 16. The FFT captures all the frequencies below the BPF. The clean, hub-radial and tip-radial inflow conditions have a fundamental stall cell frequency of 0.0625BPF, whereas the circumferential distortion condition has a fundamental stall cell frequency of 0.125BPF. For all the inflow conditions, harmonics associated with the stall cell frequency are observed up to 0.625BPF, while a region of no excitation is seen at frequencies from 0.625BPF to 0.875BPF. Close to the BPF, at 0.875BPF and 0.9375BPF, further frequency excitations are observed. This means that both low- and high-frequency disturbances are observed within the fully developed stall regime. The instabilities observed close to the BPF represent an independent phenomenon occurring in the stall regime. The obtained FFT further indicates that the fluid energy largely corresponds to low frequencies during fully developed stall.

The wavelet power spectra shown in Fig. 17 illustrate the flow physics as the stage progresses to stall. Because the initial instability that appears before stall has a frequency close to the BPF, it can be concluded that the associated fluid phenomenon that triggers the stall is initially attached to the blade surface, probably at the tip region[32]. This disturbance is shed from the blade surface and subsequently stretches to frequencies much lower than the BPF as the stage moves close to stall. For instance, the initial disturbance for the clean inflow condition (highlighted by a red dashed circle in the wavelet power spectra) appears at a time corresponding to −8 rotor revolutions and corresponds to a frequency close to the BPF. As the stage moves close to stall, this disturbance migrates to lower frequencies, the trace of which is marked by a dashed arrow in the wavelet power spectra. Therefore, the fluid phenomenon propagates at a speed close to the blade rotational speed while it is on the blade surface prior to fully developed stall, but as the fluid phenomenon sheds from the blade, it loses the momentum of the blade and gradually propagates at a slower speed. Therefore, this fluid phenomenon that triggers stall initially has a high frequency, but the frequency reduces as the phenomenon sheds from the blade. It can also be observed that the frequency of the disturbances during fully developed stall for the simple circumferential distortion inflow condition is higher compared with the clean inflow condition. Moreover, a strong low-frequency LLSD is observed for the simple circumferential distortion inflow condition.

https://doi.org/10.1017/aer.2020.120 Published online by Cambridge University Press

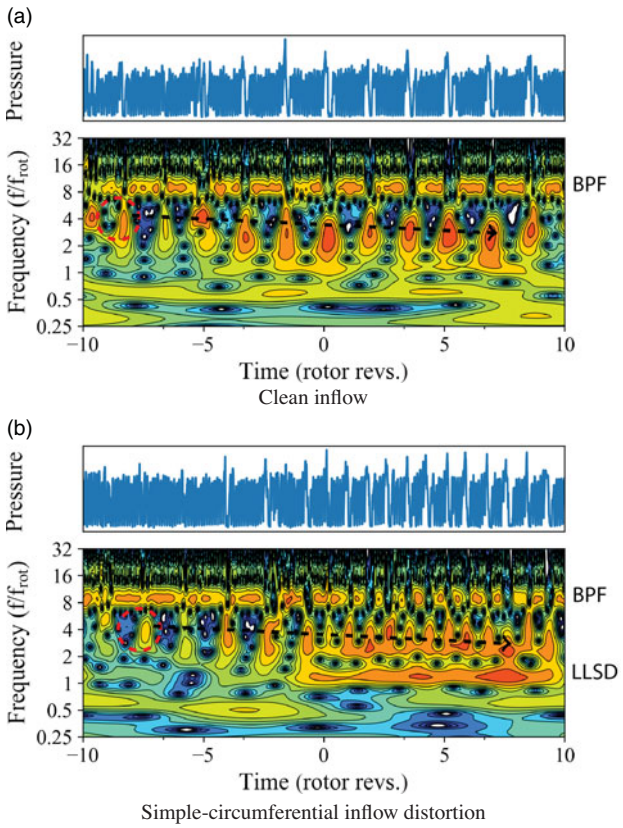

Figure 17. Wavelet power spectra during stall inception. Data were recorded at the rotor-1 leading edge at θ 90°. The dashed red circle shows the high-frequency phenomenon, while the dashed black arrow indicates the phenomenon stretching to lower frequencies.

4.0 CONCLUSIONS

This study provides an understanding of the individual contributions of the two rotors to the performance and the stall inception characteristics of a contra-rotating axial fan. Both an understanding of the stall inception and the relative contribution of the two rotors to the performance will help designers to choose better strategies to mitigate stall and improve the performance of such fans.

This paper summarises the performance and flow development across the stage of a contra-rotating fan in the design and off-design operating conditions. Different inflow conditions, namely clean, hub-radial distortion, tip-radial distortion and simple circumferential distortion inflow conditions, are investigated. The contribution of rotor-1 to the stage loading is comparatively higher than that of rotor-2. Rotor-2 stalls much earlier than rotor-1, indicating the initiation of partial stall of the stage. The loading coefficient across rotor-2 therefore starts to drop from a flow coefficient higher than the design flow coefficient, and this is observed for all inflow conditions. Inflow distortions affect the performance of both rotors individually, but rotor-1 is more severely affected as the distortion impacts directly on it. Among all the inflow

https://doi.org/10.1017/aer.2020.120 Published online by Cambridge University Press

conditions, the tip-radial distortion inflow condition shows a slightly higher loading than the hub-radial distortion condition for rotor-1 at all flow coefficients. The circumferential extent of the distortion is spread to the annulus as the flow develops across rotor-1, while the circumferential loading profiles remain nearly uniform at the exit of rotor-1. Thus the effect of distortion is felt less at the rotor-2 inlet. Significant pre-stall disturbances are captured on rotor-1, and the frequency of these disturbances increases as the stage moves towards stall. Fully developed stall is triggered by a high-frequency fluid phenomenon, which is probably attached to the blade surface. This fluid phenomenon sheds from the blade and propagates at lower frequencies during fully developed stall. Thus, the nature of the fully developed stall is characterised by significant low-frequency waves and a few high-frequency waves.

REFERENCES

1. HEIKURINEN, K. and TOWNSEND, P. PRATT and WHITNEY CANADA CORP, Low hub-to-tip ratio fan for a turbofan gas turbine engine. U.S. Patent 9,303,589, 2019.
2. WENNERSTROM, A.J. Low aspect ratio axial flow compressors: Why and what it means, *J. Turbomach.*, 1989, **111**, (4), pp 357–365.
3. GUNN, E.J. and HALL, C.A. Aerodynamics of boundary layer ingesting fans, ASME Turbo Expo 2014, Vol. 45578, pp V01AT01A024.
4. GIULIANI, J.E. and CHEN, J.P. Fan response to boundary-layer ingesting inlet distortions, *AIAA J.*, 2016, **54**, (10), pp 3232–3243.
5. MENNICKEN, M., SCHNWEITZ, D., SCHNOES, M. and SCHNELL, R. Conceptual fan design for boundary layer ingestion, Turbo Expo 2019, Vol. 58578, pp V02CT41A009.
6. PEROVIC, D., HALL, C.A. and GUNN, E.J. Stall inception in a boundary layer ingesting fan, *J. Turbomach.*, 2019, **141**, (9), pp 091007.
7. GRAY, J.S. and MARTINS, J.R. Coupled aeropropulsive design optimisation of a boundary-layer ingestion propulsor, *Aeronaut. J.*, 2019, **123**, (1259), pp 121–137.
8. EMMONS, H.W. Compressor surge and stall propagation, *Trans. ASME*, 1955, **77**, (4), pp 455–467.
9. MOORE, F.K. A theory of rotating stall of multistage compressors: Part I-III, *J. Eng. Gas Turbines Power Trans. ASME*, 1984, 106, pp 313–349.
10. MCDOUGALL N.M., CUMPSTY N.A. and HYNES T.P. Stall inception in axial compressors, *J. Turbomach.*, 1990, **112**, (1), pp 116–123.
11. GARNIER, V.H., EPSTEIN, A.H. and GREITZER, E.M. Rotating waves as a stall inception indication in axial compressors, *J. Turbomach.*, 1991, **113**, (2), pp 290–301.
12. DAY, I.J., Stall inception in axial flow compressors, *J. Turbomach.*, 1993, **115**, (1), pp 1–9.
13. CAMP, T.R. and DAY, I.J. A Study of Spike and Modal Stall Phenomena in a Low-Speed Axial Compressor, Paper no. 97-GT-526, 1998, pp V001T03A109.
14. SHARMA, P.B., JAIN, Y.P. and PUNDHIR, D.S. A study of some factors affecting the performance of a contra-rotating axial compressor stage, *Proc. Inst. Mech. Eng. Part A Power Process Eng.*, 1988, 202, (1), pp 15–21.
15. ROY, B., RAVIBABU, K., RAO, P.S., BASU, S., RAJU, A. and MURTHY P.N. Flow studies inducted twin-rotor contra-rotating axial flow fans, ASME 1992 international gas turbine and aeroengine congress and exposition, Paper no. 92-GT-390, pp V001T01A131.
16. NOURI, H., RAVELET, F., BAKIR, F., SARRAF, C. and REY, R. Design and experimental validation of a ducted counter-rotating axial-flow fans system, *J. Fluids Eng.*, 2012, **134**, (10), pp 104504.
17. CHEN, Y.Y., LIU, B., XUAN, Y. and XIANG, X.R. A study of speed ratio affecting the performance of a contra-rotating axial compressor, *Proc. Inst. Mech. Eng. Part G J. Aerospace Eng.*, 2008, **222**, (7), pp 985–991.
18. MISTRY, C. and PRADEEP, A.M. Effect of variation in axial spacing and rotor speed combinations on the performance of a high aspect ratio contra-rotating axial fan stage, *Proc. Inst. Mech. Eng. Part A J. Power Energy*, 2013, **227**, (2), pp 138–146.
19. TOGE, T.D. and PRADEEP, A.M. Experimental investigation of stall inception of a low speed contra rotating axial flow fan under circumferential distorted flow condition, *Aerospace Sci. Tech.*, 2017, **70**, pp 534–548.

https://doi.org/10.1017/aer.2020.120 Published online by Cambridge University Press

20. TOGE, T.D. and PRADEEP, A.M. Experimental investigation of stall inception and its propagation in a contra rotating axial fan under radial inflow distortion, ASME Turbo Expo 2017, Paper no. GT2017-63432, pp V02DT46A006.
21. MANAS, M.P. and PRADEEP, A.M. Stall inception mechanisms in a contra-rotating fan operating at different speed combinations, *Proc. Inst. Mech. Eng. Part A J. Power Energy*, 2019, **234**, (8), pp 1041–1052.
22. EHRICH, F. Circumferential inlet distortions in axial flow turbomachinery, *J. Aeronaut. Sci.*, 1957, **24**, (6), pp 413–417.
23. SANDERCOCK, D.M. and SANGER, N.L. Some observations of the effects of radial distortions on performance of a transonic rotating blade row, *NASA TN D-7842*, 1974, pp 1–48.
24. SCHMIDT, J.F. and RUGGERI, R.S. Performance with and without inlet radial distortion of a transonic fan stage designed for reduced loading in the tip region, *NASA-TP-1294*, 1978.
25. HAH, C., RABE, D.C., SULLIVAN, T.J. and WADIA, A.R. Effects of inlet distortion on the flow field in a transonic compressor rotor, *J. Turbomach.*, 1998, **120**, (2), pp 233–246.
26. COUSINS, W.T. and DAVIS, M.W. Evaluating complex inlet distortion with a parallel compressor model: Part 1-Concepts, theory, extensions, and limitations, ASME Turbo Expo 2011, Paper no. GT2011-45067, pp 1–12.
27. COUSINS, W.T. and DAVIS, M.W. Evaluating complex inlet distortion with a parallel compressor model: Part 2-Applications to complex patterns, ASME Turbo Expo 2011, Paper no. GT2011-45068, pp 13–23.
28. GUNN, E.J., TOOZE, S.E., HALL, C.A. and COLIN, Y. An experimental study of loss sources in a fan operating with continuous inlet stagnation pressure distortion, *J. Turbomach.*, 2013, **135**, (5), pp 051002.
29. YANG, B. and GU, C.G. The effects of radially distorted incident flow on performance of axial-flow fans with forward-skewed blades, *J. Turbomach.*, 2013, **135**, (1), pp 011039.
30. MISTRY, C. and PRADEEP, A.M. Experimental Study of the effect of radially distorted inflow on a contra-rotating fan stage, *Int. J. Rotating Mach.*, 2014, **2014**, pp 503579.
31. MISTRY, C. and PRADEEP, A.M. Influence of circumferential inflow distortion on the performance of a low speed, high aspect ratio contra rotating axial fan, *J. Turbomach.*, 2014, **136**, (7), pp 071009.
32. MANAS, M.P. and PRADEEP, A.M. Understanding unsteady flow behaviour in a low aspect ratio contra-rotating axial fan under radially distorted inflow, ASME Turbo Expo 2019, Paper no. GT2019-90252, pp V02AT45A003.
33. TO, H.O. and MILLER, R.J. The effect of aspect ratio on compressor performance, *J. Turbomach.*, 2019, **141**, (8), pp 081011.
34. TORRENCE, C. and COMPO, G.P. A practical guide to wavelet analysis, *Bull. Am. Meteorol. Soc.*, 1998, **79**, (1), pp 61–78.

https://doi.org/10.1017/aer.2020.120 Published online by Cambridge University Press